

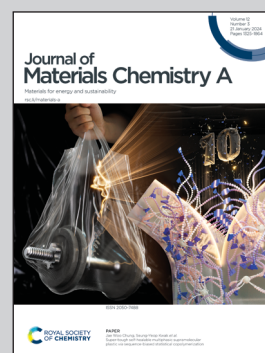


Highlighting the synthesis of the first COF based on BOPHY dye (IEC-2) for solar-driven hydrogen production by a group of researchers led by Dr Víctor A. de la Peña O'Shea from the Photoactivated Processes Unit at IMDEA Energy, Spain.

A covalent organic framework based on BOPHY/TiO₂ hybrid photocatalysts for solar driven hydrogen production










Light-driven chemistry opens the door to one promising solution towards a sustainable alternative in the current energy scenarios. Here, we describe a new and robust BOPHY-COF, highly active for direct solar hydrogen production. The high performance of the hybrid heterojunction IEC-2@T-10 results in an enhancement of the photonic efficiency, increased by 36% with respect to benchmark TiO₂. These results lay the basis for the use of these materials in the development of solar energy technologies.

As featured in:



See Teresa Naranjo, Marta Liras, Víctor A. de la Peña O'Shea *et al.*, *J. Mater. Chem. A*, 2024, 12, 1476.

PAPER

[View Article Online](#)
[View Journal](#) | [View Issue](#)Cite this: *J. Mater. Chem. A*, 2024, **12**, 1476A covalent organic framework based on BOPHY/
TiO₂ hybrid photocatalysts for solar driven
hydrogen production†Tania Mazuelo, ^a Teresa Naranjo, ^{*a} Miguel Gomez-Mendoza, ^a
Alejandro Herrero Pizarro, ^a Laura Collado, ^a Mariam Barawi, ^a
Felipe Gándara, ^b Marta Liras ^{*a} and Víctor A. de la Peña O'Shea ^{*a}

The conversion of sunlight into chemical energy to produce solar hydrogen opens the door to one promising solution towards a sustainable alternative in the current energy crisis. Herein, we describe the successful synthesis of the first COF based on BOPHY dye (IEC-2) ever reported in the literature. Its β -ketoenamine linkage confers outstanding chemical stability for light-driven applications. The hybrid photocatalyst based on IEC-2 and TiO₂ (10 wt% of COF loading) was studied for solar hydrogen evolution at both the lab-scale, and semi-pilot plant scale under natural sunlight. IEC-2@T-10 achieved a hydrogen production of 180.9 $\mu\text{mol g}^{-1}$ under 6 h solar illumination, which increased by 36% with respect to that of benchmark TiO₂. The high performance of IEC-2@T-10 results in a greater photonic efficiency than that of TiO₂ (0.12% and 0.08%, respectively), highlighting the robustness of the BOPHY COF for light-mediated reactions.

Received 17th October 2023
Accepted 17th November 2023

DOI: 10.1039/d3ta06314c

rsc.li/materials-a

1 Introduction

The fast depletion of fossil energy sources and quick global climate change force the development of key technologies to overcome these problems. The conversion of solar energy into storable and transportable solar fuels has emerged as a sustainable alternative; and photocatalytic water splitting for hydrogen production is one of the green ways to perform this energy conversion.^{1–3}

Since the first report of photocatalytic water splitting on TiO₂ electrodes by Fujishima and Honda in 1972, scientists all over the world have been making enormous efforts to improve this process. Recently, organic semiconductors have emerged as promising materials for the photocatalytic hydrogen evolution reaction (HER).^{4,5} In this sense, poly(*p*-phenylene) was the first organic photocatalyst reported for the HER.⁶ From then on, more active organic materials have been explored such as linear conjugated polymers,^{7,8} carbon nitrides,^{4,9} conjugated porous/microporous polymers (CPPs/CMPs)^{10–12} and, hybrids thereof such as metal organic frameworks (MOFs),^{13–15} among others.

Recently, the excellent photocatalytic activity of semi-conducting 2D polymers has attracted the attention of the scientific community. Thanks to the 2D planar structure, 2D polymers present unique characteristics such as large surface active sites, porous structures, efficient charge separation and migration, and high modularity as a singular platform for the construction of heterostructures.^{16–18} Thereby, various organic polymers with a 2D structure have been investigated for the photocatalytic HER from water.^{19–22} In this context, we can find an emerging class of porous and crystalline materials, covalent organic frameworks (COFs), which present distinguished relevance in various areas such as gas storage and separation,^{23,24} heterogeneous catalysis,^{25–28} energy storage and optoelectronic devices.^{29–31}

In 2014 Lotst and coworkers reported the first COF, a hydrazone-based COF, active in the photocatalytic HER.³² This promising study was the starting point for the development of new COF-based photocatalysts, and the field has quickly grown in the last decade.³³ 2D COFs with extended π - π conjugated structures have demonstrated great potential for application in photocatalysis, as they exhibit adequate and tunable optoelectronic properties and great conductivity along the whole structure.

In this sense, the development of COFs and their heterostructures with inorganic semiconductors has attracted the attention of the scientific community.^{34,35} These hybrids can improve charge separation and the presence of COFs bears synthetic versatility. In this respect, the design and synthesis of novel COFs and hybrids thereof are crucial. A smart design

^aIMDEA Energy Institute, Av/Ramón de la Sagra, 3 Móstoles, Madrid E-28935, Spain.
E-mail: teresa.naranjo@imdea.org; marta.liras@imdea.org; victor.delapenya@imdea.org

^bInstituto de Ciencia de Materiales de Madrid (ICMM-CSIC), C/Sor Juana Inés de la Cruz, 3, Madrid E-28049, Spain

† Electronic supplementary information (ESI) available. See DOI: <https://doi.org/10.1039/d3ta06314c>

leads to improved light harvesting and charge separation to push the photocatalytic activity. In the last few years, we have witnessed huge growth of the COF field, looking for new strategies for the simultaneous combination of crystallinity, stability and functionality.^{33,36} In this line, presence of nitrogen-based linkages increased chemical stability,^{37,38} and the β -ketoenamine-linked COFs exhibit unique features and outstanding chemical stability³⁹ to be exploited as photocatalysts for H_2 production.⁴⁰ These COFs are assembled by the direct condensation of triformylphloroglucinol (**Tp**) with multifunctional amines, after a first step of imine formation followed by an irreversible tautomerization, which leads to an enhanced stability.

One of the most remarkable advantages of 2D COFs is that their electronic structure can be tuned at the molecular level by modulating the organic building block, awarding unique properties to the material. In this regard, BOPHY (boron pyrrol hydrazine) is a new class of fluorescent dye reported for the first time in 2014.^{41,42} It presents two chelating positions amenable for linking boron. Thus, the synthetic access to this dye involves boron chelation of a π -conjugated dipyrrole-based system, including a central hydrazine-based spacer. BOPHY dyes are excellent photoactive materials suitable for several applications in different fields such as solar cells,^{43,44} analytical chemistry,⁴⁵ and electrochemistry,⁴⁶ among others. In fact, we have reported the synthesis of BOPHY-based CPPs as photocatalysts for oxidation of organic sulfides,⁴⁷ hydrogen production,⁴⁸ CO_2 photoreduction,⁴⁹ and also as part of a photon up-conversion system.⁵⁰ However, to the best of our knowledge there are no examples in the literature for COFs containing BOPHY dye as the main moiety in their molecular structure.

Herein, we report the design and synthesis of a β -ketoenamine COF based on BOPHY dye, **IEC-2** (IEC stands for an IMDEA Energy COF). We use this new crystalline and stable material to prepare an organic–inorganic hybrid photocatalyst incorporating **IEC-2** and TiO_2 , namely **IEC-2@T-10**. The photocatalytic activity of the hybrid material has been studied in HER experiments at the lab-scale, reaching a hydrogen production of *ca.* $720 \mu\text{mol g}^{-1} \text{h}^{-1}$ (photonic efficiency ξ 0.27%) in the absence of any noble metal co-catalyst. This hybrid photocatalyst was scaled up and studied in a semi-pilot plant solar reactor located in the IMDEA Energy Institute, achieving a hydrogen production of $180.9 \mu\text{mol g}^{-1}$ under 6 h of solar illumination and 0.12% photonic efficiency. The charge transfer mechanism between TiO_2 and **IEC-2** has been elucidated by means of field emission scanning electron microscopy (FESEM), time-resolved photoluminescence and transient absorption spectroscopy (TAS).

2 Experimental

2.1 Preparation of photocatalysts

2.1.1 Synthesis of IEC-2. The synthesis of IEC-2 is described in Scheme 1. Thus, 2,7-diamino BOPHY (**2**) (15.4 mg, 0.04 mmol, see ESI,[†] Section 2 for more details) and 1,3,5-triformylphloroglucinol (**Tp**) (5.9 mg, 0.03 mmol) were sonicated in a Pyrex tube (o.d. \times i.d. = $16 \times 17 \text{ mm}^2$ and length 18 cm)

containing 1.4 mL of BuOH/mesitylene 1:1 for 10 minutes. Then 140 μL acetic acid (10% v/v) was added. The mixture was then bubbled with argon for 15 minutes. The tube was sealed and heated at 100 $^\circ\text{C}$ for 4 days. The product obtained was filtered and washed with MeOH and DCM. **IEC-2** (19 mg, 97%) was obtained as a bright garnet solid. Solid ^{13}C NMR (400 MHz) δ 190.9, 181.2, 174.1, 148.5, 136.5, 126.8, 212.5, 106.4, 100.4, 10.6 ppm.

2.1.2 Synthesis of the IEC-2@T-10 hybrid material. For the preparation of hybrid materials, first, TiO_2 was calcined at 400 $^\circ\text{C}$ for 4 h to remove all possible adsorbed organic impurities. Then, both TiO_2 and **IEC-2** (using 10 wt% of COF loading) were mixed with a mortar and pestle. Afterwards, they were transferred to a round bottom flask and a mixture of acetonitrile/water (ACN/ H_2O) 1:1 v/v was added. The mixture was sonicated for 2 minutes, and then the solvents were removed using a rotary evaporator at 45 $^\circ\text{C}$. The hybrid was dried and mixed again with a mortar and pestle.

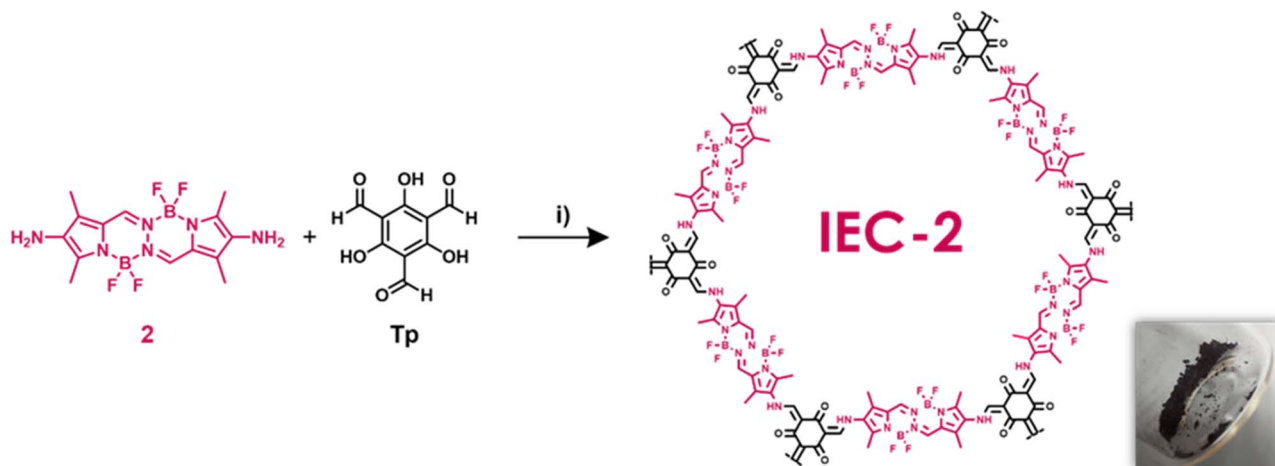
For the elucidation of the charge transfer mechanism, **IEC-2@T-10** was decorated with Pt nanoparticles. The metal nanoparticles were photodeposited *in situ* by dissolving an appropriate amount of $H_2PtCl_6 \cdot H_2O$ to obtain 3 wt% Pt nominal loading on the same solution used to carry out the lab scale hydrogen production assay (*vide infra*) and then irradiated for 5 minutes.

2.2 Advanced characterization

2.2.1 Photoelectrochemical characterization. The photoelectrodes were prepared by drop casting an **IEC-2** suspension on gold coated glasses. The COF was dispersed with an ultrasound tip on isopropanol with a 4 mg mL^{-1} concentration. The experiments were performed in a three-electrode configuration in a photoelectrochemical cell with a quartz window containing an aqueous solution of 0.5 M Na_2SO_3 (pH = 9). An Ag/AgCl electrode was employed as the reference electrode, a Pt wire was used as the counter electrode and IEC-2 samples, as the working electrode. These experiments were performed with a potentiostat-galvanostat Autolab PGSTAT204 provided with an integrated impedance module FRAII (using 10 mV modulation amplitude, from 0.1–106 Hz). A solar simulator (a LOT LSH302 Xe lamp and an LSZ389 AM1.5 global filter) calibrated to 1 Sun (100 mW cm^{-2}) was used as a light source. The exposed area of the photoelectrode to the electrolyte was 1 cm^2 .

2.2.2 Steady-state and time-resolved photoluminescence spectroscopy. Steady-state photoluminescence experiments for the solid powdered samples were carried out with a fluorescence spectrometer PerkinElmer LS 55, with an excitation wavelength of 300 nm and using a cut-off filter at 350 nm in front-face mode.

Time-resolved photoluminescence was recorded with a Mini Tau system provided from Edinburgh Instruments. A laser diode EPL-375 was used as the excitation source at $\lambda_{\text{exc}} = 372 \text{ nm}$ (pulse width of 61.2 ps). A band-pass filter in the range of 425–475 nm was employed to accurately monitor the photoluminescence of the TiO_2 signal. The instrument response function (IRF) signal was measured as the reference in all cases.



Scheme 1 Chemical synthesis of IEC-2. (i) BuOH/mesitylene 1 : 1, AcOH 10% v/v, 100 °C, 4 days.

The corresponding fitting curves were adjusted by using mono exponential functions.

2.2.3 Transient absorption spectroscopy (TAS). TAS measurements were carried out with an LP980-K laser from Edinburgh Instruments based on an optical parametric oscillator (OPO) pumped by the third harmonic ($\lambda_{\text{exc}} = 355$ nm) of a Nd:YAG laser (EKSPLA). Single low energy pulses of 1 mJ per pulse of *ca.* 5 ns duration were employed, and a pulsed xenon flash lamp (150 W) was employed as the detecting light source. The probe light is dispersed through a monochromator (TMS302-A, grating 150 lines per mm) after it has passed the sample, and then it reaches a PMT detector (Hamamatsu Photonics) to obtain the temporal profile. The absorbance of all samples was kept at ~ 0.2 at $\lambda_{\text{exc}} = 355$ nm as dispersed aqueous solutions containing 10% of methanol (v/v). All transient spectra were recorded at room temperature using 1×1 cm quartz cells which were bubbled for 15 min with N_2 before acquisition.

2.2.4 Field emission scanning electron microscopy (FESEM). The study was performed on FESEM JEOL JSM-7900F equipment equipped with an energy-dispersive X-ray spectroscopy detector (X-EDS, Ultim Max 170 Oxford Instruments model). The images have been processed by means of Aztec of Oxford instruments software. The sample was prepared by dispersing the material in ethanol and dropped onto silicon wafers and dried.

2.3 Photocatalytic hydrogen evolution reaction tests

2.3.1 Lab-scale hydrogen production assays. Photocatalytic hydrogen production experiments were conducted in a Pyrex glass double-walled reactor. 25 mg of catalyst were added to 130 mL of 10 vol% aqueous methanol solution. The reactor was tightly closed and maintained at atmospheric pressure and 20 °C by recirculating water from a cooling system. Ar was flowed through the solution in order to purge the system and also to act as a carrier gas. Then, the solution was irradiated by using a 150 W medium-pressure Hg immersion lamp, with the H_2 evolution being monitored every 3 min by means of an

Agilent 490 micro-GC equipped with a molecular sieve column and a TCD detector.

2.3.2 Solar hydrogen production assays. Solar hydrogen production tests were performed in July 2023, in a semi-pilot plant gas-phase photoreactor (Fig. S18†) located at IMDEA Energy Institute (Móstoles, Madrid, Spain). The photoreactor consists of a concentric Pyrex glass tube ($L = 50$ cm, $\phi_{\text{inner}} = 0.3$ cm, $\phi_{\text{outer}} = 0.5$ cm), coupled to a compound parabolic collector (CPC) and is mounted on a fixed platform tilted by 35° (local latitude, UTM 30 N 425173.88 4465847.24) towards the south to maximize light absorption. The total irradiated area is 0.12 m² and the total irradiated volume is 0.1 L. For the experiments, catalysts (0.3 g) were coated on the inner glass tube using aqueous suspensions. The photoreactor was fed in continuous mode with a humid argon flow (50 mL min⁻¹), after bubbling an aqueous methanol solution (10 vol% methanol) at 60 °C. The reactor was kept in the dark until the air was completely removed, and then it was uncovered and kept under sunlight for 6 h. Hydrogen evolution was detected using an Agilent 490 micro-GC, equipped with a MS5A column and a TCD detector. Solar UVA radiation intensity (300–400 nm wavelength) was measured using a radiometer (ACADUS 85-PLS) mounted on a platform at the same angle as the CPC. Data were recorded every minute and referred to received energy (W m⁻²).

3 Results and discussion

3.1 Design, synthesis and characterization of IEC-2

We have designed and synthesized for the first time a β -ketoenamine COF based on BOPHY dye (IEC-2, Scheme 1). For this aim, we use as building blocks, triformylphloroglucinol (**Tp**) and a non-commercial 2,7-diamino BOPHY monomer (**2**), not reported before in the literature (Scheme S1 and Fig. S1–S4†). The reaction mechanism can be divided into two steps: in the first reversible step, **Tp** is condensed with **2**. In the second step, an irreversible tautomeric equilibrium, between the enol-

imine and ketoenamine isomers, is strongly displaced to the more stable ketoenamine tautomer.

The structure of **IEC-2** was investigated based on computer modellization along with analysis of the experimental powder X-ray diffraction (PXRD) data (Fig. 1 and S6†). The PXRD pattern of **IEC-2** shows several broad peaks, as commonly found for two-dimensional COFs, with the most intense one being at $2\theta = 3.46^\circ$. The formation of honeycomb (hcb) layers was thus assumed based on the connectivity of the BOPHY and **Tp** building units, and supported by the spectroscopically demonstrated (*vide infra*) enamine bond formation. Several crystal models were completed accordingly and geometrically optimized, beginning with the default hexagonal symmetry (ESI,† Section 5). A crystal structure model with monoclinic *Cm* symmetry and lattice parameters $a = 33.68 \text{ \AA}$, $b = 8.56 \text{ \AA}$, and $c = 28.84 \text{ \AA}$, $\beta = 118.61$ was found to be the one that best describes the experimental powder diffraction pattern (Fig. 1). In this crystal model, the 6-member rings within the layers are slightly distorted, and the layers stack along the crystallographic *b* axes with a staggered sequence (Fig. 1B and C). While the limited crystallinity of the sample prevents the completion of further structural refinements or determination of any possible stacking order, the proposed model explains the position of the observed diffraction peaks based on the expected formation of extended layers. Accordingly, the peak at $2\theta = 3.45^\circ$ is assigned to the (001) plane ($d = 25.32 \text{ \AA}$), while the peak centered at $2\theta = 11.0^\circ$ would be contributed by both the (202) and the (11–1) planes ($d = 8.14 \text{ \AA}$ and 7.92 \AA , respectively). Fourier-transform infrared (FTIR) and solid-state ^{13}C cross-polarization magic angle spinning nuclear magnetic resonance (CP-MAS NMR) data collected for **IEC-2** clearly confirm that the tautomerism is completely shifted to the ketoenamine isomer. First, FTIR spectra revealed the appearance of two important signals. A band associated with the C=O stretching mode of the ketone in the backbone of the COF is observed at 1647 to 1595 cm^{-1} , and a signal located at 1299 cm^{-1} is ascribed to an enamine C–N stretching band (Fig. 2A). Additionally, the FTIR spectra

confirmed the complete condensation between the two building blocks by the disappearance of the bands at 3350 and 3200 cm^{-1} , which are assigned to the primary amine stretching bands (Fig. 2A). Additional confirmation of the complete condensation of the building blocks is obtained from solid state NMR (Fig. 2B). ^{13}C CP-MAS NMR data collected for **IEC-2** showed signals at 190.9 , 181.2 and 174.1 ppm , assigned to the ketone carbon. These three signals come from the same carbonyl group with three different chemical environments. Furthermore, signals assigned to the aldehyde (*ca.* 192.3 ppm) and hydroxyl carbon (*ca.* 174.4 ppm) functional groups of **Tp** are no longer visible (Fig. S5†). This demonstrates that the Schiff-base reaction of the building blocks and the tautomerization of the hydroxyl group take place. On the other hand, the signal at 148.5 ppm is assigned to the carbon alpha to the amine. Moreover, due to BOPHY's skeleton, the **IEC-2** spectrum shows peaks in the region of 136 to 106 ppm , while the methyl carbon atoms show a broad peak at 10.6 ppm .

Field emission scanning electron microscopy (FESEM) images (Fig. 2C and D) show that **IEC-2** crystallizes with a flower-like morphology, assembled from flake petals, exhibiting lengths in the nanometre range. The porous nature of **IEC-2** was evaluated by N_2 adsorption and desorption measurements, and its surface area was calculated by BET (Brunauer–Emmett–Teller) theory (Fig. S7†). Thus, **IEC-2** shows a BET surface area of $56 \text{ m}^2 \text{ g}^{-1}$.

The pore size distribution was calculated with non-local density functional theory (NLDFT). It had narrow pore size distributions of 1.0 – 1.7 nm exhibiting a maximum at 1.5 nm (Fig. S8†). The thermal stability of **IEC-2** was analysed by thermogravimetric analysis (TGA) under an air atmosphere (Fig. S9†). The thermogram shows a complete mass loss at 200°C , a value slightly lower than that of other BOPHY-based CPPs described by us.⁴⁸

Regarding the electronic structure, electrochemical studies helped to estimate the relative energy levels of the HOMO/LUMO of **IEC-2**. According to the oxidation and reduction



Fig. 1 (A) PXRD patterns of **IEC-2**: experimental (red), calculated (blue) and the Bragg positions (green). (B) Top view and (C) lateral view of AB stacking of **IEC-2**.



Fig. 2 (A) FTIR spectrum of IEC-2 and FTIR spectra of its starting materials for reference. (B) Solid-state ¹³C CP/MAS NMR of IEC-2 and theoretical assignment. (C and D) FESEM images of IEC-2.

potentials (1.48 and -0.64 V vs. Ag/Ag^+ , respectively) obtained from cyclic voltammetry (CV) measurements (Fig. S11[†]), the HOMO was estimated to be -5.5 eV, and the LUMO was -3.4 eV (Fig. 3A), resulting in an electrochemical bandgap energy of 2.1 ± 0.3 eV (see the ESI[†] for the ferrocene correction performed to achieve these values). The optical measurements carried out by UV-vis diffuse reflected spectroscopy confirm that IEC-2 exhibits an indirect transition of 1.9 ± 0.1 eV. Fig. S11,† in agreement with the measured electrochemical band gap.

Electrochemical impedance spectroscopy (EIS) was carried out at different bias potentials and the Mott-Schottky plot was obtained by calculating the associated capacitance of the electrode-electrolyte interface. The determination of the flat band potential was achieved from this plot and it was correlated with the Fermi level position,^{51,52} which has been determined to be at 0.8 V vs. NHE (Fig. 3B). Furthermore, the negative slope of this plot revealed p-type conductivity of IEC-2.

The photoactive properties of IEC-2 were measured by photovoltage experiments, confirming that the p-type conductivity observed by the EIS measurements, showing an increase in the signal under illumination (Fig. 3C).⁵³

In this sense, the photoresponse of the electrode is -130 mV under illumination at open circuit potential. Moreover, a linear sweep voltammetry measurement under chopped illumination (Fig. 3D) confirms the photoactivity of this material and exhibits a wide range of potentials with negative photocurrents. This agrees well with previous results and confirms the potential of this material to be used as a photocathode.

At this point, we wondered if we would be able to design a p-n heterojunction hybrid material using IEC-2 as a p type semiconductor and TiO_2 , which is a very well-known n-type semiconductor.

So, a hybrid material was prepared by using a wet mixture of TiO_2 (PC500, anatase phase) and IEC-2 at 10 wt% of COF loading, and named IEC-2@T-10. This loading percentage was

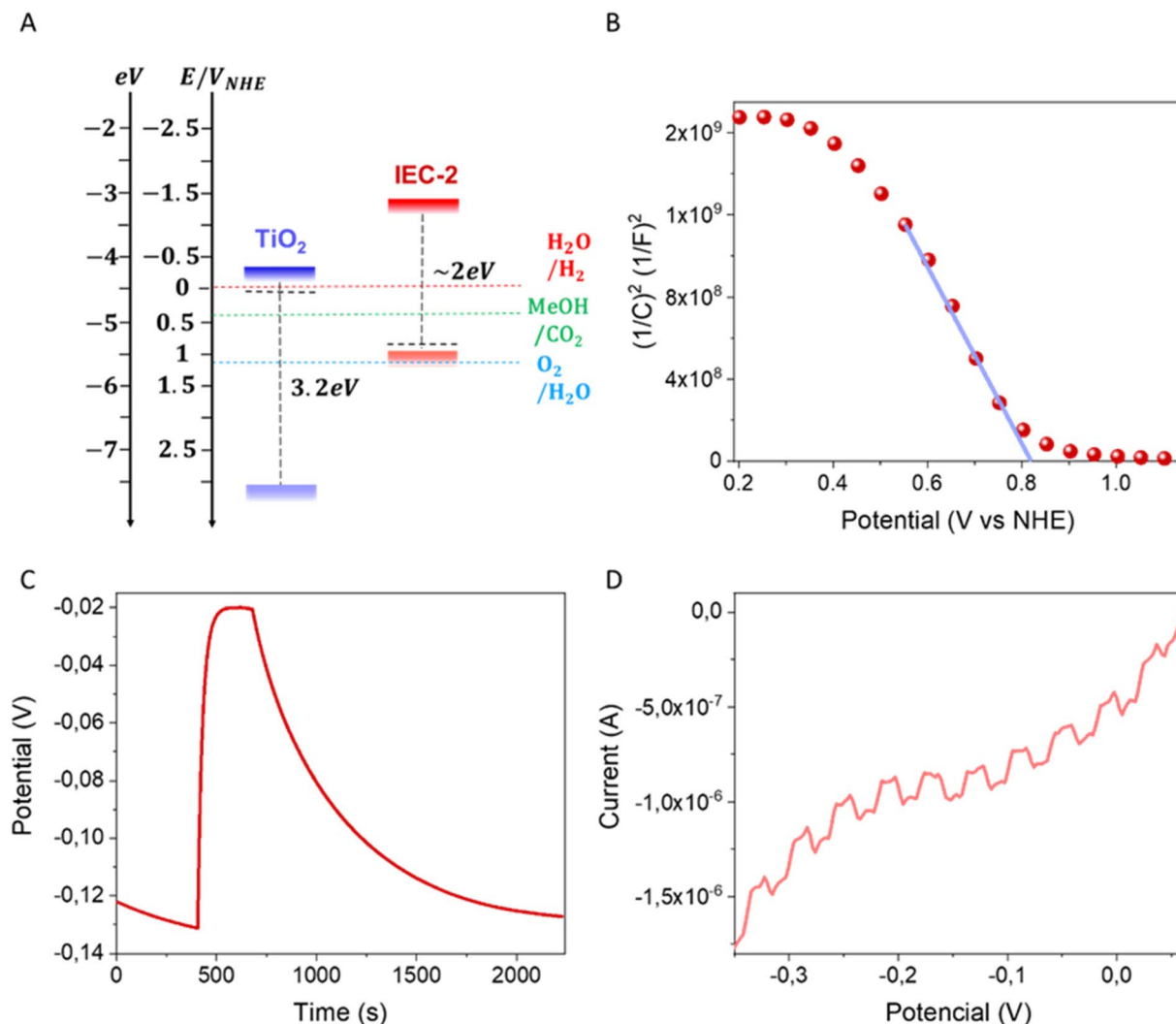


Fig. 3 (A) Band energy diagram obtained for IEC-2 (TiO_2 is included for comparative purposes), including the water-splitting redox couples at pH = 0 (NHE). Dotted lines represent the Fermi level positions for both materials. (B) Mott-Schottky plot of IEC-2, and (C) photovoltage and (D) linear sweep voltammetry under chopped illumination of IEC-2.

selected considering our previous experience.^{48,49,54} The percentage weight of the COF was determined by thermogravimetric analyses (Fig. S10†).

The morphology of the hybrid system was studied by FESEM and X-EDS microanalysis confirming that the crystalline BOPHY COF particles are homogeneously surrounded by the TiO_2 nanocrystals (Fig. 4). These results show that the IEC-2@ TiO_2 composite has a large interface leading to a short carrier migration distance. Furthermore, the porous IEC-2 structure provides a high number of active sites and light absorption ability.

3.2 Photocatalytic activity for the HER

3.2.1 Lab scale experiments. The photocatalytic activity of IEC-2 and its hybrid material based on TiO_2 , IEC-2@T-10, was evaluated in the production of hydrogen from water in the absence of any noble metal co-catalyst and using methanol as the sacrificial agent. The COF by itself showed a moderate

performance ($\xi = 0.02\%$). However, the synergetic effect between both organic and inorganic counterparts in the heterojunction, IEC-2@T-10, resulted in a hydrogen evolution rate of $\approx 720 \mu\text{mol g}_{\text{cat}}^{-1} \text{h}^{-1}$ ($\xi = 0.27\%$), which was more than 14 and 9 times greater than those of IEC-2 and TiO_2 , respectively (Fig. 5A). This value is in the same range as that of other hybrid photocatalysts based on BOPHY-conjugated porous polymers.⁴⁸

The photochemical stability of the hybrid material was studied in two recycling experiments. In the first photocatalytic run, after 5 hours of illumination, the hybrid material was filtered and redispersed to be studied in a long cycle of 24 h (Fig. 5B). No sign of catalyst deactivation was observed, which demonstrates that the robust 2D crystalline structure of IEC-2 confers excellent photostability to the hybrid to be reusable. In the second recycling experiment, after 8 UV-light (ON-OFF) cycles, again, no loss of activity was observed (Fig. S14†). At the same time, the structural stability was confirmed by means of

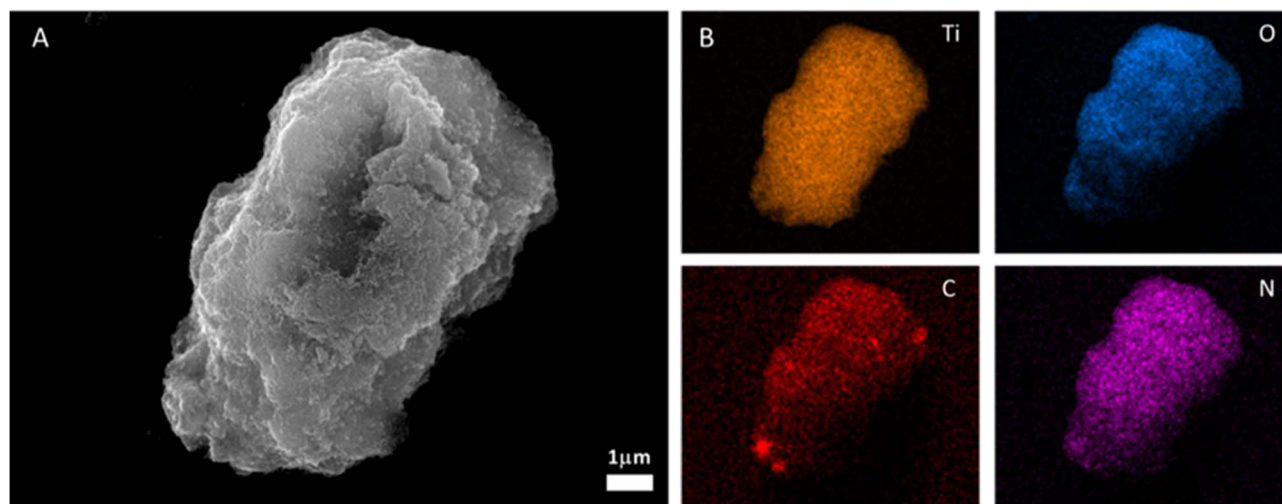


Fig. 4 FESEM of the IEC-2@T-10 sample: (A) SEM image. (B) X-EDS microanalysis images of image A showing titanium (orange), oxygen (blue), carbon (red), and nitrogen (purple).

FTIR spectra before and after the photocatalytic tests (Fig. S15†).

3.2.2 Solar-driven experiments. The good result obtained in lab-scale experiments encouraged us to test IEC-2@T-10 in a close to real system, such as a semi pilot plant photoreactor. Fig. 6 shows the gas-phase solar hydrogen production from an aqueous methanol solution (10 vol% methanol) under solar illumination. In all cases, H_2 production is referred to the received energy to allow a direct data comparison. IEC-2@T-10 successfully achieved a hydrogen evolution rate of $41.5 \mu\text{mol h}^{-1} \text{g}^{-1}$ in scaling-up tests (Fig. 6A), and a cumulative production of $180.9 \mu\text{mol g}^{-1}$ after 6 h of sunlight illumination (Fig. 6B). Interestingly, the photocatalytic activity of IEC-2@T-10 increased by 36% with respect to that of bare TiO_2 (Fig. 6B), corroborating the beneficial effect of combining both semiconductors to promote hydrogen evolution.

Indeed, a good proof of performance enhancement is also the increase in the photonic efficiency of the hybrid over TiO_2 (0.12% and 0.08%, respectively). The high photocatalytic activity of the hybrid agrees well with the trend obtained at the laboratory scale, and is an indication of the robustness of the BOPHY COF for light-driven reactions. It is important to highlight that there are no examples in the literature about the use of this kind of hybrid material for solar hydrogen evolution at the semi-pilot plant scale.

3.3 Elucidation of the charge-transfer mechanism

To unravel the charge-transfer pathway in the heterojunction IEC-2@T-10, we have carried out spectroscopic studies from the ns to μs timescale by means of transient absorption spectroscopy (TAS), and from the ps to ns timescale through time-resolved photoluminescence (TRPL). First of all, the influence of the COF over TiO_2 in the hybrid was evaluated through TAS

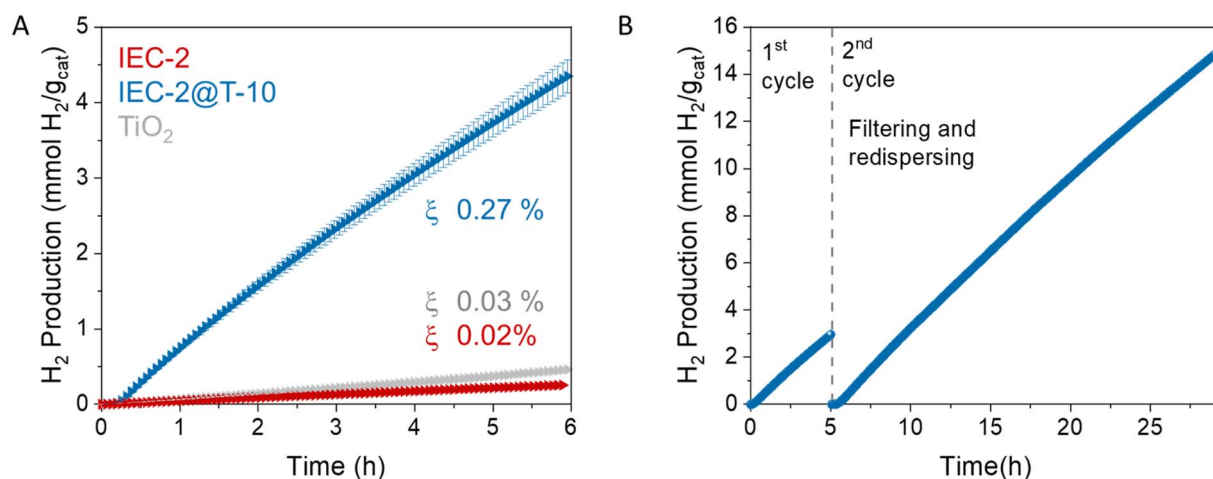


Fig. 5 (A) Cumulative H_2 production vs. time (h) of IEC-2 (red), IEC-2@T-10 (blue) and bare TiO_2 (grey) under UV illumination. Photonic efficiencies are included for reference. (B) Long duration recycling experiment using IEC-2@T-10 as the photocatalyst for H_2 production.

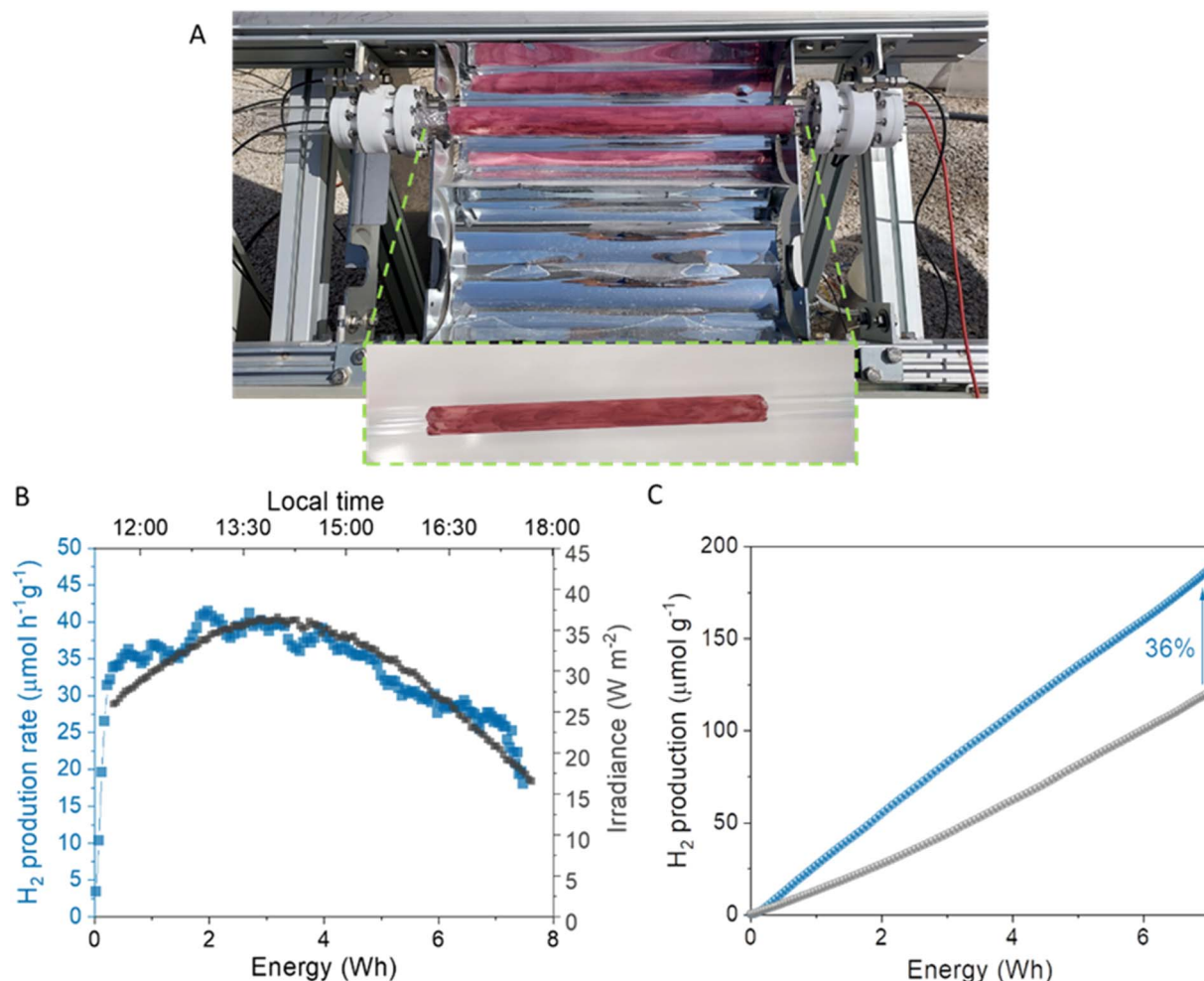


Fig. 6 (A) Semi-pilot plant solar CPC reactor and zoomed-in view of the tubular reactor coated with the IEC-2@T-10 hybrid. (B) Hydrogen evolution rate ($\mu\text{mol h}^{-1} \text{g}^{-1}$) of IEC-2@T-10 vs. received solar energy. The variation of the solar irradiance (UVA) along the experiment and the elapsed time are also plotted for comparison. (C) Cumulative solar H_2 production of IEC-2@T-10 (blue) and bare TiO_2 (grey) under equivalent received energy conditions.

($\lambda_{\text{exc}} = 355 \text{ nm}$). The samples were investigated in 10 vol% methanol aqueous solution to ensure the same conditions as those employed in the photocatalytic tests (Fig. 5).

After excitation, bare TiO_2 showed a continuous TA spectrum in the whole visible spectral range, exhibiting a small band at $\approx 460 \text{ nm}$ in agreement with previously reported results using ns-TAS systems (Fig. 7A).^{54,55} Since methanol is a very efficient hole scavenger,^{56–58} the measured TiO_2 signal under our conditions (*ca.* between 400 and 650 nm) can be only attributed to photoelectrons.^{55,59–61} A bare IEC-2 COF showed low transient absorption upon 30 ns after a laser pulse, exhibiting two maxima ΔOD at 450 and from 600 nm with identical kinetic profiles (Fig. 7A and S17† for a comparison of its dynamic profile at different λ of detection). Regarding the IEC-2@T-10 hybrid (Fig. 7A and S18†), a marked increase in terms of ΔOD was observed in the visible spectral window during the first 100 ns after a pulse with respect to bare TiO_2 . This finding suggests that a synergy effect occurs in the heterojunction, which favors

a decrease in the electron–hole recombination in the hybrid due to the presence of the COF.

The comparative of the kinetic profiles ($\lambda_{\text{exc}} = 355 \text{ nm}$ and $\lambda_{\text{obs}} = 460 \text{ nm}$ where TiO_2 exhibit the transient maximum) for IEC-2@T-10 and the naked materials revealed a huge growth of its transient lifetime (τ_{TAS}) of 2- or 7-fold compared to that of TiO_2 or IEC-2, respectively (Fig. 7B and S19†). In addition, a delay in the ΔOD maximum was observed for the hybrid up to 20 ns after the laser pulse (Fig. 7B). We have previously observed this finding in hybrids composed of TiO_2 and CPPs based on BOPHY, BODIPY or benzyl functionalized truxene,^{48,49,62} when a type II heterojunction charge-transfer takes place (Fig. 7D). We observed that TiO_2 showed two main contributions: $\tau_{\text{TAS}} \approx 52$ and 785 ns (Fig. S20†), by fitting the kinetic curves by means of mono- or bi-exponential functions.

On the other hand, IEC-2@T-10 exhibited a noticeable increase in the same two main contributions: $\tau_{\text{TAS}} \approx 100$ and 875 ns (Fig. S20†), confirming a slowing-down of the electron–hole pair recombination process in the hybrid (Fig. 7B). Note



Fig. 7 (A) Transient absorption spectra ($\lambda_{\text{exc}} = 355$ nm) for TiO₂ (grey), IEC-2@T-10 (blue) and IEC-2 (red) in deaerated 10 vol% aqueous methanol suspensions at different time scales (30, 100 and 500 ns after the laser pulse). (B) Corresponding transient decay lifetimes ($\lambda_{\text{exc}} = 355$ nm and $\lambda_{\text{obs}} = 460$ nm) for TiO₂ (grey), IEC-2@T-10 (blue) and IEC-2 (red) under the same conditions. (C) Time-resolved photoluminescence ($\lambda_{\text{exc}} = 372$ nm, $\lambda_{\text{obs}} = 425\text{--}475$ nm) for TiO₂ (grey), IEC-2@T-10 (blue) and IEC-2 (red) in the solid state. The instrument response function (IRF) is included. (D) Proposed type II heterojunction charge-transfer mechanism for the hybrid based on TiO₂ as an inorganic semiconductor and the COF IEC-2 as the organic counterpart.

that the sum of the lifetimes of titania and the COF (Fig. S21†) would be lower than the value observed for the hybrid ($\tau_{\text{TAS}} \approx 100$ ns). In addition, the kinetic profile for the hybrid and the pristine materials remains unaltered from 100 ps to 5 ns after the pulse, following the enhancement of the heterojunction's signal through a charge transfer process in the ns–μs scale. This result highlights the importance of the synergy between the inorganic–organic counterparts to improve the photocatalytic efficiency.

Furthermore, time-resolved photoluminescence (TRPL) experiments were performed to corroborate the charge-transfer process from the COF to titania (Fig. 7C). A band-pass filter centered at 450 nm (where TiO₂ emits, see Fig. S22†) was employed to monitor only the influence of the COF over TiO₂ in the hybrid. Under these conditions, naked titania (3.40 ns) shows lower TRPL than TiO₂ forming part of the hybrid IEC-

2@T-10 (3.85 ns, see the corresponding fitting in Fig. S23†). Note that a pristine COF is not fluorescent, and then the TRPL is negligible under the selected window of measurement. The combination of the results extracted from TAS and TRPL clearly shows a slower recombination of the TiO₂'s dynamic charge in the hybrid, meaning that the charge transfer process occurs from the COF's LUMO to the conduction band of TiO₂ following a type II mechanism.

To support the proposed mechanism, the hybrid IEC-2@T-10 was decorated with 3 wt% of Pt nanoparticles by photo-deposition and analyzed by FESEM experiments (Fig. S24†). Upon analysis using a Robinson-type backscatter detector (BED-C) for Z-contrast (atomic number), Pt-3/IEC-2@T-10 shows the preferential photodeposition of Pt nanoparticles on the TiO₂ surface (brilliant points in Fig. S14B† and its magnification C). This finding was also corroborated by means of energy-

dispersive X-ray spectroscopy (X-EDS) mapping (Fig. S24D†) where the platinum nanoparticles can be clearly distinguished above TiO₂ nanocrystals rather than the COF counterpart. In addition, EDS analysis showed the presence of platinum up to 3.7% (Fig. S24D†). As the photodeposition of platinum nanoparticle follows a photoreduction pathway, this means that the preferred surface where the reduction takes place is TiO₂. These results, combined with those determined by photophysical techniques, indicate that the photocatalytic reduction takes place over the TiO₂ surface.

4 Conclusions

In summary, this work reports for the first time the successful synthesis of a β -ketoenamine COF based on BOPHY dye. For this aim, a new 2,7-diamino BOPHY molecule has been described to be used as a building block for the COF's synthesis. A crystal structure consisting of AB-stacked layers with a staggered sequence has been proposed.

Furthermore, this crystalline COF has been used as a platform to prepare a hybrid organic–inorganic heterojunction based on TiO₂ (**IEC-2@T-10**). The photocatalytic performance of **IEC-2** and the hybrid photocatalyst was tested in the HER under lab scale conditions, reaching 41 $\mu\text{mol g}^{-1} \text{h}^{-1}$ ($\xi = 0.02\%$) and 720 $\mu\text{mol g}^{-1} \text{h}^{-1}$ ($\xi = 0.27\%$) respectively. The scaling up of the hybrid material was accomplished in a gas-phase CPC solar reactor in the absence of any noble metal cocatalyst. The hybrid **IEC-2@T-10** achieved a photocatalytic hydrogen production of 180.9 $\mu\text{mol g}^{-1}$ ($\xi = 0.12\%$) under 6 h of solar illumination, which was 36% higher than that of TiO₂. The synergy effect between the organic and the inorganic counterparts was corroborated by spectroscopic studies, revealing a type II heterojunction mechanism.

The new BOPHY-COF described here and its associated 2,7-diaminobophy linking monomer, both open up a new avenue for the rational synthesis of novel photo(electro)catalysts and hybrid heterostructures, with potential for application in a multitude of light-driven energy processes.

Conflicts of interest

There are no conflicts to declare.

Acknowledgements

Financial support was received from the national projects N-GREEN (PID2022-141688OB-I00), SOLFuture (PLEC2021-007906), SOLARCHEM5.0 (TED2021-130173B-C41), ARMONIA (PID2020-119125RJ-I00), NOVACO2 (PID2020-118593RB-C21), MATERIALIZATION (PID2021-123287OB-I00) and SolarCPP-Bat (CNS2022-135380) funded by MCIN/AEI/10.13039/501100011033. T. M. and M. B. thank the Spanish MICIN for the FPI (PRE2020-094445_FPI20) and the Juan de la Cierva Incorporación (IJC2019 – 042430-I) grants, respectively.

References

- 1 J. H. Alstrum-Acevedo, M. K. Brennaman and T. J. Meyer, Chemical Approaches to Artificial Photosynthesis. 2, *Inorg. Chem.*, 2005, **44**(20), 6802–6827.
- 2 N. S. Lewis and D. G. Nocera, Powering the Planet: Chemical Challenges in Solar Energy Utilization, *Proc. Natl. Acad. Sci.*, 2006, **103**(43), 15729–15735.
- 3 H. J. Sayre, L. Tian, M. Son, S. M. Hart, X. Liu, D. M. Arias-Rotondo, B. P. Rand, G. S. Schlau-Cohen and G. D. Scholes, Solar Fuels and Feedstocks: The Quest for Renewable Black Gold, *Energy Environ. Sci.*, 2021, **14**, 1402–1419.
- 4 X. Wang, K. Maeda, A. Thomas, K. Takanabe, G. Xin, J. M. Carlsson, K. Domen and M. Antonietti, A Metal-Free Polymeric Photocatalyst for Hydrogen Production from Water under Visible Light, *Nat. Mater.*, 2009, **8**(1), 76–80.
- 5 G. Zhang, Z.-A. Lan and X. Wang, Conjugated Polymers: Catalysts for Photocatalytic Hydrogen Evolution, *Angew. Chem., Int. Ed. Engl.*, 2016, **55**(51), 15712–15727.
- 6 S. Yanagida, A. Kabumoto, K. Mizumoto, C. Pac and K. Yoshino, Poly(p-Phenylene)-Catalysed Photoreduction of Water to Hydrogen, *J. Chem. Soc., Chem. Commun.*, 1985, **8**, 474–475.
- 7 D. J. Woods, R. S. Sprick, C. L. Smith, A. J. Cowan and A. I. Cooper, A Solution-Processable Polymer Photocatalyst for Hydrogen Evolution from Water, *Adv. Energy Mater.*, 2017, **7**(22), 1700479.
- 8 R. S. Sprick, B. Bonillo, M. Sachs, R. Clowes, J. R. Durrant, D. J. Adams and A. I. Cooper, Extended Conjugated Microporous Polymers for Photocatalytic Hydrogen Evolution from Water, *Chem. Commun.*, 2016, **52**(65), 10008–10011.
- 9 K. Schwinghammer, M. B. Mesch, V. Duppel, C. Ziegler, J. Senker and B. V. Lotsch, Crystalline Carbon Nitride Nanosheets for Improved Visible-Light Hydrogen Evolution, *J. Am. Chem. Soc.*, 2014, **136**(5), 1730–1733.
- 10 M. Barawi, L. Collado, M. Gomez-Mendoza, F. E. Oropeza, M. Liras and V. A. Peña O'Shea, Conjugated Porous Polymers: Ground-Breaking Materials for Solar Energy Conversion, *Adv. Energy Mater.*, 2021, 2101530.
- 11 C. Yang, B. C. Ma, L. Zhang, S. Lin, S. Ghasimi, K. Landfester, K. A. I. Zhang and X. Wang, Molecular Engineering of Conjugated Polybenzothiadiazoles for Enhanced Hydrogen Production by Photosynthesis, *Angew. Chemie*, 2016, **128**(32), 9348–9352.
- 12 L. Li, Z. Cai, Q. Wu, W.-Y. Lo, N. Zhang, L. X. Chen and L. Yu, Rational Design of Porous Conjugated Polymers and Roles of Residual Palladium for Photocatalytic Hydrogen Production, *J. Am. Chem. Soc.*, 2016, **138**(24), 7681–7686.
- 13 B. Zhu, R. Zou and Q. Xu, Metal–Organic Framework Based Catalysts for Hydrogen Evolution, *Adv. Energy Mater.*, 2018, **8**(24), 1–33.
- 14 A. García-Sánchez, M. Gomez-Mendoza, M. Barawi, J. I. Villar-García, M. Liras, F. Gándara and V. A. de la Peña O'Shea, Fundamental Insights in Photoelectrocatalytic

- Hydrogen Production with a Hole-Transport Bismuth Metal-Organic Framework, *J. Am. Chem. Soc.*, 2020, **142**, 318–326.
- 15 X. Chen, S. Xiao, H. Wang, W. Wang, Y. Cai, G. Li, M. Qiao, J. Zhu, H. Li, D. Zhang and Y. Lu, MOFs Conferred with Transient Metal Centers for Enhanced Photocatalytic Activity, *Angew. Chem., Int. Ed.*, 2020, **59**(39), 17182–17186.
 - 16 J. Low, S. Cao, J. Yu and S. Wageh, Two-Dimensional Layered Composite Photocatalysts, *Chem. Commun.*, 2014, **50**(74), 10768–10777.
 - 17 X. Wang, S. Blechert and M. Antonietti, Polymeric Graphitic Carbon Nitride for Heterogeneous Photocatalysis, *ACS Catal.*, 2012, **2**(8), 1596–1606.
 - 18 W. J. Ong, L. L. Tan, Y. H. Ng, S. T. Yong and S. P. Chai, Graphitic Carbon Nitride (g-C₃N₄)-Based Photocatalysts for Artificial Photosynthesis and Environmental Remediation: Are We a Step Closer to Achieving Sustainability?, *Chem. Rev.*, 2016, **116**(12), 7159–7329.
 - 19 S. Cao, J. Low, J. Yu and M. Jaroniec, Polymeric Photocatalysts Based on Graphitic Carbon Nitride, *Adv. Mater.*, 2015, **27**(13), 2150–2176.
 - 20 J. Zhang, Y. Wang, J. Jin, J. Zhang, Z. Lin, F. Huang and J. Yu, Efficient Visible-Light Photocatalytic Hydrogen Evolution and Enhanced Photostability of Core/Shell CdS/g-C₃N₄ Nanowires, *ACS Appl. Mater. Interfaces*, 2013, **5**(20), 10317–10324.
 - 21 Q. Tang, Y.-Y. Gu, J. Ning, Y. Yan, L. Shi, M. Zhou, H. Wei, X. Ren, X. Li, J. Wang, C. Tang, L. Hao and J. Ye, Boosting Photocatalysis of Hydrazone-Linked Covalent Organic Frameworks through Introducing Electron-Rich Conjugated Aldehyde, *Chem. Eng. J.*, 2023, **470**, 144106.
 - 22 X. Guan, Y. Qian, X. Zhang and H.-L. Jiang, Enaminone-Linked Covalent Organic Frameworks for Boosting Photocatalytic Hydrogen Production, *Angew. Chem., Int. Ed.*, 2023, **62**(31), e202306135.
 - 23 P. Das and S. K. Mandal, In-Depth Experimental and Computational Investigations for Remarkable Gas/Vapor Sorption, Selectivity, and Affinity by a Porous Nitrogen-Rich Covalent Organic Framework, *Chem. Mater.*, 2019, **31**(5), 1584–1596.
 - 24 S. S. Han, H. Furukawa, O. M. Yaghi and W. A. Goddard, Covalent Organic Frameworks as Exceptional Hydrogen Storage Materials, *J. Am. Chem. Soc.*, 2008, **130**(35), 11580–11581.
 - 25 H. Lyu, C. S. Diercks, C. Zhu and O. M. Yaghi, Porous Crystalline Olefin-Linked Covalent Organic Frameworks, *J. Am. Chem. Soc.*, 2019, **141**(17), 6848–6852.
 - 26 S. Lin, C. S. Diercks, Y.-B. Zhang, N. Kornienko, E. M. Nichols, Y. Zhao, A. R. Paris, D. Kim, P. Yang, O. M. Yaghi and C. J. Chang, Covalent Organic Frameworks Comprising Cobalt Porphyrins for Catalytic CO₂ Reduction in Water, *Science*, 2015, **349**(6253), 1208–1213.
 - 27 R. Chen, J.-L. Shi, Y. Ma, G. Lin, X. Lang and C. Wang, Designed Synthesis of a 2D Porphyrin-Based Sp² Carbon-Conjugated Covalent Organic Framework for Heterogeneous Photocatalysis, *Angew. Chem., Int. Ed.*, 2019, **58**(19), 6430–6434.
 - 28 S. Yan, X. Guan, H. Li, D. Li, M. Xue, Y. Yan, V. Valtchev, S. Qiu and Q. Fang, Three-Dimensional Salphen-Based Covalent–Organic Frameworks as Catalytic Antioxidants, *J. Am. Chem. Soc.*, 2019, **141**(7), 2920–2924.
 - 29 S. Wan, J. Guo, J. Kim, H. Ihee and D. Jiang, A Belt-Shaped, Blue Luminescent, and Semiconducting Covalent Organic Framework, *Angew. Chem., Int. Ed.*, 2008, **47**(46), 8826–8830.
 - 30 Z. Meng, R. M. Stolz and K. A. Mirica, Two-Dimensional Chemiresistive Covalent Organic Framework with High Intrinsic Conductivity, *J. Am. Chem. Soc.*, 2019, **141**(30), 11929–11937.
 - 31 L. Wang, C. Zeng, H. Xu, P. Yin, D. Chen, J. Deng, M. Li, N. Zheng, C. Gu and Y. Ma, A Highly Soluble, Crystalline Covalent Organic Framework Compatible with Device Implementation, *Chem. Sci.*, 2019, **10**(4), 1023–1028.
 - 32 L. Stegbauer, K. Schwinghammer and B. V. Lotsch, A Hydrazone-Based Covalent Organic Framework for Photocatalytic Hydrogen Production, *Chem. Sci.*, 2014, **5**(7), 2789–2793.
 - 33 F. Haase and B. V. Lotsch, Solving the COF Trilemma: Towards Crystalline, Stable and Functional Covalent Organic Frameworks, *Chem. Soc. Rev.*, 2020, **49**(23), 8469–8500.
 - 34 D. Wang, X. Li, L. L. Zheng, L. M. Qin, S. Li, P. Ye, Y. Li and J. P. Zou, Size-Controlled Synthesis of CdS Nanoparticles Confined on Covalent Triazine-Based Frameworks for Durable Photocatalytic Hydrogen Evolution under Visible Light, *Nanoscale*, 2018, **10**(41), 19509–19516.
 - 35 Y. Wang, P. Dong, K. Zhu, A. Zhang, J. Pan, Z. Chen, Z. Li, R. Guan, X. Xi and J. Zhang, Embedding [Mo₃S₁₃]^{2−} Clusters into the Micropores of a Covalent Organic Framework for Enhanced Stability and Photocatalytic Hydrogen Evolution, *Chem. Eng. J.*, 2022, **446**, 136883.
 - 36 W. Zhang, L. Chen, S. Dai, C. Zhao, C. Ma, L. Wei, M. Zhu, S. Y. Chong, H. Yang, L. Liu, Y. Bai, M. Yu, Y. Xu, X.-W. Zhu, Q. Zhu, S. An, R. S. Sprick, M. A. Little, X. Wu, S. Jiang, Y. Wu, Y.-B. Zhang, H. Tian, W.-H. Zhu and A. I. Cooper, Reconstructed Covalent Organic Frameworks, *Nature*, 2022, **604**(7904), 72–79.
 - 37 C. R. DeBlase and W. R. Dichtel, Moving Beyond Boron: The Emergence of New Linkage Chemistries in Covalent Organic Frameworks, *Macromolecules*, 2016, **49**(15), 5297–5305.
 - 38 J. L. Segura, M. J. Mancheño and F. Zamora, Covalent Organic Frameworks Based on Schiff-Base Chemistry: Synthesis, Properties and Potential Applications, *Chem. Soc. Rev.*, 2016, **45**(20), 5635–5671.
 - 39 S. Kandambeth, A. Mallick, B. Lukose, M. V. Mane, T. Heine and R. Banerjee, Construction of Crystalline 2D Covalent Organic Frameworks with Remarkable Chemical (Acid/Base) Stability via a Combined Reversible and Irreversible Route, *J. Am. Chem. Soc.*, 2012, **134**(48), 19524–19527.
 - 40 L.-J. Wang, P.-Y. Dong, G. Zhang and F.-M. Zhang, Review and Perspectives of β -Keto-Enamine-Based Covalent Organic Framework for Photocatalytic Hydrogen Evolution, *Energy Fuels*, 2023, **37**(9), 6323–6347.
 - 41 C. Yu, L. Jiao, P. Zhang, Z. Feng, C. Cheng, Y. Wei, X. Mu and E. Hao, Highly Fluorescent BF₂ Complexes of Hydrazone-

- Schiff Base Linked Bispyrrole, *Org. Lett.*, 2014, **16**(11), 3048–3051.
- 42 I.-S. Tamgho, A. Hasheminasab, J. T. Engle, V. N. Nemykin and C. J. Ziegler, A New Highly Fluorescent and Symmetric Pyrrole–BF₂ Chromophore: BOPHY, *J. Am. Chem. Soc.*, 2014, **136**(15), 5623–5626.
 - 43 A. Mirloup, Q. Huaulmé, N. Leclerc, P. Lévêque, T. Heiser, P. Retailleau and R. Ziessel, Thienyl-BOPHY Dyes as Promising Templates for Bulk Heterojunction Solar Cells, *Chem. Commun.*, 2015, **51**(79), 14742–14745.
 - 44 Q. Huaulmé, A. Mirloup, P. Retailleau and R. Ziessel, Synthesis of Highly Functionalized BOPHY Chromophores Displaying Large Stokes Shifts, *Org. Lett.*, 2015, **17**(9), 2246–2249.
 - 45 X.-D. Jiang, Y. Su, S. Yue, C. Li, H. Yu, H. Zhang, C.-L. Sun and L.-J. Xiao, Synthesis of Mono-(p-Dimethylamino)Styryl-Containing BOPHY Dye for a Turn-on PH Sensor, *RSC Adv.*, 2015, **5**(22), 16735–16739.
 - 46 H. M. Rhoda, K. Chanawanno, A. J. King, Y. V. Zatsikha, C. J. Ziegler and V. N. Nemykin, Unusually Strong Long-Distance Metal–Metal Coupling in Bis(Ferrocene)-Containing BOPHY: An Introduction to Organometallic BOPHYs, *Chem.–Eur. J.*, 2015, **21**(50), 18043–18046.
 - 47 C. G. López-Calixto, S. Cabrera, R. Pérez-Ruiz, M. Barawi, J. Alemán, V. A. de la Peña O'Shea and M. Liras, Conjugated Porous Polymer Based on BOPHY Dyes as Photocatalyst under Visible Light, *Appl. Catal., B*, 2019, **258**, 117933.
 - 48 C. G. López-Calixto, M. Barawi, M. Gomez-Mendoza, F. E. Oropeza, F. Fresno, M. Liras and V. A. De La Peña O'Shea, Hybrids Based on BOPHY-Conjugated Porous Polymers as Photocatalysts for Hydrogen Production: Insight into the Charge Transfer Pathway, *ACS Catal.*, 2020, **10**(17), 9804–9812.
 - 49 L. Collado, T. Naranjo, M. Gomez-Mendoza, C. G. López-Calixto, F. E. Oropeza, M. Liras, J. Marugán and V. A. de la Peña O'Shea, Conjugated Porous Polymers Based on BODIPY and BOPHY Dyes in Hybrid Heterojunctions for Artificial Photosynthesis, *Adv. Funct. Mater.*, 2021, **31**(51), 2105384.
 - 50 C. G. López-calixto, M. Liras, V. A. De, P. O. Shea and R. Pérez-ruiz, Environmental Synchronized Biphotonic Process Triggering C-C Coupling Catalytic Reactions, *Appl. Catal., B*, 2018, **237**, 18–23.
 - 51 F. Cardon and W. P. Gomes, On the Determination of the Flat-Band Potential of a Semiconductor in Contact with a Metal or an Electrolyte from the Mott-Schottky Plot, *J. Phys. D: Appl. Phys.*, 1978, **11**(4), L63.
 - 52 M. Orazem and B. Tribollet, *Electrochemical Impedance Spectroscopy*, Wiley-Interscience, New York, 2008.
 - 53 M. Barawi, E. Alfonso-González, C. G. López-Calixto, A. García, A. García-sánchez, I. J. Villar-García, M. Liras and V. A. de la Peña O'Shea, Advanced Nanostructured Conjugated Microporous Polymer Application in a Tandem Photoelectrochemical Cell for Hydrogen Evolution Reaction, *Small*, 2022, 2201351.
 - 54 M. Gomez-mendoza, M. Pintado-sierra, C. Monterde, M. Barawi, F. Sánchez, M. Iglesias, V. A. De, P. O. Shea and M. Liras, Hybrid Photocatalyst for Hydrogen Production : The Effect of Fluorine on Optoelectronic Properties of Conjugated Porous Polymers, *Adv. Sustain. Syst.*, 2022, **2200160**, 1–11.
 - 55 A. O. T. Patrocinio, J. Schneider, M. D. França, L. M. Santos, B. P. Caixeta, A. E. H. Machado and D. W. Bahnemann, Charge Carrier Dynamics and Photocatalytic Behavior of TiO₂ Nanopowders Submitted to Hydrothermal or Conventional Heat Treatment, *RSC Adv.*, 2015, **5**(86), 70536–70545.
 - 56 H. Liu, M. Liu, R. Nakamura and Y. Tachibana, Primary Photocatalytic Water Reduction and Oxidation at an Anatase TiO₂ and Pt-TiO₂ Nanocrystalline Electrode Revealed by Quantitative Transient Absorption Studies, *Appl. Catal., B*, 2021, **296**, 120226.
 - 57 A. Yamakata, T. Ishibashi and H. Onishi, Effects of Water Addition on the Methanol Oxidation on Pt/TiO₂ Photocatalyst Studied by Time-Resolved Infrared Absorption Spectroscopy, *J. Phys. Chem. B*, 2003, **107**(36), 9820–9823.
 - 58 T. Yoshihara, R. Katoh, A. Furube, Y. Tamaki, M. Murai, K. Hara, S. Murata, H. Arakawa and M. Tachiya, Identification of Reactive Species in Photoexcited Nanocrystalline TiO₂ Films by Wide-Wavelength-Range (400–2500 Nm) Transient Absorption Spectroscopy, *J. Phys. Chem. B*, 2004, **108**(12), 3817–3823.
 - 59 V. N. Kuznetsov and N. Serpone, Visible Light Absorption by Various Titanium Dioxide Specimens, *J. Phys. Chem. B*, 2006, **110**(50), 25203–25209.
 - 60 R. Katoh, M. Murai and A. Furube, Transient Absorption Spectra of Nanocrystalline TiO₂ Films at High Excitation Density, *Chem. Phys. Lett.*, 2010, **500**(4–6), 309–312.
 - 61 J. Schneider, M. Matsuoka, M. Takeuchi, J. Zhang, Y. Horiuchi, M. Anpo and D. W. Bahnemann, Understanding TiO₂ photocatalysis: Mechanisms and Materials, *Chem. Rev.*, 2014, **114**(19), 9919–9986.
 - 62 A. Valverde-González, C. G. López Calixto, M. Barawi, M. Gomez-Mendoza, V. A. de la Peña O'Shea, M. Liras, B. Gómez-Lor and M. Iglesias, Understanding Charge Transfer Mechanism on Effective Truxene-Based Porous Polymers–TiO₂ Hybrid Photocatalysts for Hydrogen Evolution, *ACS Appl. Energy Mater.*, 2020, **3**, 4411–4420.